Journal of Materials Research and Technology 42 (2026) 10750–10759

Contents lists available at ScienceDirect

Journal of Materials Research and Technology

journal homepage: www.elsevier.com/locate/jmrt

Atmosphere-controlled thermal processing enables tunable optical properties via iron-oxide phase engineering in natural silicate materials

Álvaro Urbaneja-Miguel [b], Alba Torija-López [a], Ángel Carrancho [c], Eneko Iriarte [d], Sara Gonzalez-Moreno [b], Jose Manuel Gonzalez-Martin [b], Miriam Trigo-Lopez [a], Saúl Vallejos [a,*]

[a] Departamento de Química, Facultad de Ciencias, Universidad de Burgos, Plaza Misael Bañuelos s/n, 09001, Burgos, Spain
[b] Departamento de Construcciones Arquitectónicas e Ingeniería de la Construcción y del Terreno, Escuela Politécnica Superior, Universidad de Burgos, C/ Villadiego s/n, 09001, Burgos, Spain
[c] Área de Prehistoria, Departamento de Historia, Geografía y Comunicación. Universidad de Burgos, Edificio I+d+i. Plaza Misael Bañuelos s/n, 09001, Burgos, Spain
[d] IsoTOPIK Lab, Área de Paleontologia, Departamento de Historia, Geografía y Comunicación, Universidad de Burgos, Edificio de I+d+i, Plaza Misael Bañuelos s/n, 09001, Burgos, Spain

ARTICLE INFO

Keywords:
Iron-oxide phase equilibria
Redox-controlled thermal processing
Process–structure–property relationship
Magnetite–hematite transformation
Atmosphere-controlled heat treatment
Functional optical materials

ABSTRACT

Controlled-atmosphere thermal processing was investigated as a method to engineer iron-oxide phase assemblages in iron-bearing silicate materials. Natural sandstone was heated between 200 and 1000 °C under air, N_2 and CO_2 atmospheres to evaluate how oxygen partial pressure governs redox transformations and the resulting macroscopic optical behaviour.

The treatments produced a wide and reproducible range of optical responses from a single starting material. Colour evolution, quantified in the CIELAB space, correlates with bulk mineral transformations. Oxidizing conditions stabilize hematite-dominated assemblages and generate red hues, whereas reduced-oxygen atmospheres promote magnetite formation and progressive darkening. Rock-magnetic measurements identify atmosphere-dependent phase assemblages, including a high-coercivity iron oxide under strongly oxidizing conditions. The magnetic response mirrors the optical evolution, indicating that colour development originates from internal phase transformations.

Compressive strength remained within the same order of magnitude as the untreated material across the studied conditions, indicating no catastrophic mechanical degradation.

These results show that oxygen availability acts as a key processing variable controlling iron-oxide stability and optical response. The study establishes a process-based approach for tuning optical properties in mineral materials through atmosphere-controlled thermal processing without chemical additives. Unlike previous studies focused on temperature-driven effects or isolated observations, this work demonstrates a reproducible process-based approach to tune optical properties in natural silicate materials through controlled atmosphere engineering.

1. Introduction

Iron-oxide phases in silicate materials strongly influence macroscopic optical behaviour. Thermal treatments are particularly effective in modifying these phase equilibria because temperature and oxygen availability jointly control redox reactions and mineral stability fields. These transformations are governed by well-established Fe–O phase equilibria and polymorphic transitions between iron oxides, which strongly depend on temperature and oxygen partial pressure [1].

Iron-bearing clay minerals and accessory phases in silicate matrices undergo progressive transformations during heating, including dehydration, dehydroxylation and redox reactions. These processes are also associated with microstructural changes, including the partial closure of pre-existing microcracks at intermediate temperatures due to thermal expansion and stress redistribution, followed by the generation of new microcracks at higher temperatures as a result of dehydration and

* Corresponding author.
E-mail address: svallejos@ubu.es (S. Vallejos).

https://doi.org/10.1016/j.jmrt.2026.05.175
Received 12 February 2026; Received in revised form 4 May 2026; Accepted 15 May 2026
Available online 22 May 2026

structural breakdown [2,3]. These processes modify the relative stability of hematite, magnetite and related phases, which act as chromophores within the silicate matrix. Consequently, thermal processing provides a non-chemical route to modify functional properties without introducing external additives, provided that the phase evolution can be controlled reproducibly.

Previous studies on thermally treated iron-bearing silicate materials have mainly reported limited colour variations associated with oxidation of iron-bearing phases. Research on thermally exposed historical monuments shows that heat commonly induces pink or reddish-brown tones due to the oxidation of precursor iron hydroxides to hematite [4]. Other investigations have focused primarily on the mechanical behaviour of sandstones heated to high temperatures, with colour changes treated as secondary effects. These works highlight the influence of initial composition, trace elements and specific thermal-treatment conditions on final colour outcomes [5]. These trends are consistent with previous studies showing that high temperature induces microcrack development, mineral expansion and progressive degradation of mechanical properties in sandstones and other rock types [6,7].

However, despite this body of work, the role of oxygen availability as an independent and controllable processing parameter has not been systematically explored for engineering iron-oxide phase assemblages and tuning the resulting optical response. While the influence of oxygen partial pressure on iron-oxide stability is well established, its use as a process variable to reproducibly control macroscopic optical properties in natural silicate materials remains largely unexplored. In particular, frameworks linking atmosphere control, phase evolution and optical response in natural stone are still lacking. This distinction moves beyond descriptive observations by framing oxygen availability as a controllable processing parameter for tuning optical properties in natural silicate materials.

Building upon this gap, the present study examines how controlled oxygen availability modifies iron-oxide equilibria during heating. Whereas oxidizing conditions stabilize hematite-dominated assemblages, reduced-oxygen atmospheres promote magnetite formation and progressive darkening. By applying air, N_2 and CO_2 atmospheres during heating, a wide and reproducible range of macroscopic optical responses was obtained from the same starting material without chemical additives.

A comprehensive characterisation of these thermally modified samples was carried out to understand their composition, transformation pathways and material stability and mechanical response. Petrographic and petrophysical analyses provided information on microstructure and phase distribution. X-ray diffraction (XRD), X-ray fluorescence (XRF) and organic-carbon quantification (LOI) were used to determine crystalline structure, elemental composition and matrix evolution. Rock-magnetic experiments characterised ferromagnetic phase transformations under different atmospheres and temperatures. Finally, mechanical performance was evaluated through uniaxial compressive strength tests to verify that phase transformations did not induce catastrophic mechanical degradation.

The present work investigates atmosphere-controlled thermal processing as a means of engineering iron-oxide phase assemblages within an iron-bearing silicate framework. By systematically combining temperature (200–1000 °C) with different oxygen partial pressures (air, N_2, CO_2), the study evaluates how redox conditions govern mineral transformations and the resulting macroscopic optical response. A multi-technique characterization (petrographic, geochemical and rock-magnetic analyses) is used to establish a process–structure–property correlation linking thermal environment, phase evolution and optical functional properties, extending existing knowledge beyond conventional studies focused on either mechanical degradation or oxidation-driven colour changes. In contrast to highly engineered optical systems based on complex photonic architectures, such as those exploiting Fano resonances and topological photonic crystals [8], the present approach relies on controlled thermal processing of natural materials to achieve tunable optical responses without chemical additives.

2. Experimental

2.1. Materials

The sandstone used in this study corresponds to a subarkosic to lithic arenite from the fluvial facies of the Urbión Group (Wealden, Upper Jurassic–Lower Cretaceous). The material was obtained from a commercial quarry operated by Areniscas Stone (Vilviestre del Pinar, Burgos, Spain; 41.9668° N, 3.0886° W). Sampling was restricted to a single lithological unit in order to minimize variability associated with stratigraphic heterogeneity. Visibly altered, weathered, fractured or vein-rich zones were excluded during selection. All experimental specimens were cut from the selected blocks and prepared to the dimensions required for colour, petrographic, mechanical and analytical measurements, ensuring internal consistency across the experimental series.

High-purity gases were used for the thermal treatments as received: nitrogen (99.999%, Air Liquide) and carbon dioxide (99.7%, Air Liquide).

2.2. Instrumentation and general methods

Stone colour was measured using a desktop colourimeter (Konica Minolta Chroma Meter CR-5, AQ Instruments, Valencia, Spain). Cubic specimens (5 × 5 × 5 cm) were analysed, and all six faces of each cube were measured. Prior to each measurement session, the CR-5 was calibrated following the manufacturer's prescribed two-step procedure. First, a zero calibration (0% reflectance), also referred to as black calibration, was performed using the dedicated zero calibration box (CM-A124). Once installed, the instrument executed the calibration sequence, during which the xenon lamp flashed three times to establish the dark reference. Subsequently, a white calibration (100% reflectance) was carried out using the built-in certified white calibration plate integrated into the instrument. As in the zero calibration, the xenon lamp flashed three times during this process to define the white reference. This dual calibration procedure ensures accurate normalisation of the instrument response across the full reflectance range and minimises instrumental drift. Calibration was performed before each measurement session following the instrument guidelines.

Compressive-strength tests followed the EN 1926:2006 standard (Natural Stone Test Methods: Uniaxial Compressive Strength) and were performed using a universal testing machine (Servosis ME-405, 5–500 kN, Pinto, Spain). Tests were conducted on cubic specimens (50 mm side length; n = 10 per condition), and results are reported as mean values ± standard deviation.

Thin sections were prepared at the Thin Section Laboratory of CENIEH (Burgos), producing 0.036-mm-thick samples mounted on standard slides. Petrographic observations were conducted at the University of Burgos using a Nikon AZ-100 stereomicroscope and a Nikon Eclipse LV100POL polarizing microscope equipped with a Nikon DS-Fi2 digital camera. Imaging and measurements were performed with Nikon NIS-Elements software.

To complement petrographic observations, the semi-quantitative mineralogical composition (wt%) of each sample was determined by X-ray diffraction (XRD). Approximately 5 g of sandstone were powdered in an agate mortar for XRD, LOI and geochemical analyses. XRD data were collected at the Science and Technology Park of the University of Burgos using a Bruker D8 Discover Davinci A25 diffractometer (Cu tube, 40 kV, 30 mA) over a continuous 5°–70° 2θ range, with 0.05° step size and 2 s per step. Diffractograms were interpreted using DIFRAC.EVA. Phase identification by X-ray diffraction (XRD) was performed in a semi-quantitative manner based on normalized peak intensities. The detection limit for crystalline phases under these conditions is estimated to be on the order of 1–4 wt%, and values close to this threshold should be

interpreted with caution.

X-ray fluorescence (XRF) was used to obtain semi-quantitative elemental compositions (wt%). Samples were finely ground, homogenized, mixed with flux (lithium metaborate/tetraborate, 0.5% KBr), and fused into glass beads. Analyses were performed using a Thermo Electron ARL Advant XP spectrometer, and spectra were interpreted with WinXRF Advant 3.2.1. The reported oxide concentrations should be interpreted as semi-quantitative bulk elemental data. Instrument calibration was performed using the standard calibration routines available for fused-bead silicate materials; UniQuant software from Thermo XRF spectrometers is designed to enable standardless, quantitative analysis of unknown samples. UniQuant utilizes a pre-calibrated factory state, eliminating the need for application-specific calibration standards for every sample type. Because the objective of the analysis was to identify relative compositional trends among thermally treated samples, the XRF data are used comparatively (semiquantitatively) rather than as absolute high-precision elemental concentrations. Minor oxides close to the detection limit should therefore be interpreted with caution. The analytical uncertainty for major oxides is estimated to be within ±1–2% relative, consistent with typical instrumental performance for bulk silicate materials.

Loss-on-ignition (LOI) analyses were used to determine organic carbon content. Powdered samples were dehydrated at 110 °C for 14 h and subsequently calcined at 550 °C for 5 h using a programmable HD-230 PAD furnace. Mass changes were recorded after each step.

Multivariate statistical analysis of the geochemical dataset (XRF and LOI) was carried out using SPSS v.31. Principal Component Analysis (PCA) was applied to explore major trends associated with thermal treatment and atmosphere. Variables included SiO_2, Al_2O_3, K_2O, Fe_2O_3, Na_2O, TiO_2, MgO, and organic carbon (Corg). All variables were standardized prior to analysis to avoid scaling bias. PCA was computed for the full set of 19 samples.

Magnetic characterisation was performed on bulk sandstone samples (~400 mg) from each temperature–atmosphere combination described in Section 2.3. Between 1 and 3 samples per condition were analysed (16 air, 19 N_2, 9 CO_2). The objective was to assess variations in magnetic mineral type, concentration and particle size. Measurements included progressive isothermal remanent magnetization (IRM) acquisition curves, hysteresis loops (±1 T), backfield coercivity curves and thermomagnetic curves (magnetization vs. temperature in air up to 700 °C; heating/cooling rate 6–12 °C/min). Analyses were conducted using a Variable Field Translation Balance (MM_VFTB). Curie/Néel temperatures were estimated using the two-tangent method [9]. Magnetic parameters including Ms, Mrs, Bc and Bcr were interpreted with Rock_Mag_Analyzer software [10]. Hysteresis parameters (Ms, Mrs, Bc) were corrected for diamagnetic/paramagnetic contributions, while Bcr was obtained from backfield curves. All magnetic experiments were performed at the Paleomagnetism Laboratory of the University of Burgos (Spain).

2.3. Specific methods. Thermal treatment of the sandstones

The thermal treatment of the sandstone samples was carried out in a CARBOLITE CWF 12/13 furnace equipped with an Inconel A105 retort, enabling operation under controlled gas atmospheres. Samples were heated at a rate of 6 °C/min to the target temperatures (200, 400, 600, 800 or 1000 °C), held isothermally for 7 h, and then allowed to cool naturally to room temperature inside the furnace under continuous gas flow, ensuring consistent thermal history across all samples. The selected temperature range (200–1000 °C) was chosen to encompass the main thermally activated processes in the sandstone, including dehydration and dehydroxylation of clay minerals at intermediate temperatures and redox-driven transformations of iron oxides at higher temperatures, as reported in the literature [4–7]. Achieving homogeneous optical response required modification of gas-flow distribution inside the retort, highlighting the importance of gas-flow management and thermal-gradient control in atmosphere-controlled colour tuning.

For experiments conducted in air, no external gas was supplied and both inlet and outlet ports of the retort remained open to the laboratory environment. For nitrogen and CO_2 atmospheres, the retort was first purged with the corresponding gas at 4.5 L/min for 30 min prior to heating. During the heating and cooling stages, gas flow was maintained at 1.5 L/min to ensure stable atmospheric conditions throughout the process.

Two modifications were introduced into the retort to achieve homogeneous colouration of the sandstone samples. Initial tests revealed that although the gas inlet tube was located above the retort, the supplied gas entered at a temperature significantly lower than the working conditions, producing local cooling and resulting in heterogeneous colour patterns. To prevent this, a labyrinth-like internal structure was designed to preheat the gas before it contacted the stones. These structures were designed to increase the residence time of the incoming gas and promote thermal equilibration before contact with the samples. The structures consisted of stacked natural stone elements forming a tortuous flow path, with an overall height of approximately 27 cm and lateral dimension of 15 cm, matching the internal dimensions of the retort. The gas was forced to follow a multi-directional path through interconnected channels with characteristic widths of a few millimetres to centimetres, depending on the configuration, thereby enhancing heat exchange with the surrounding material.

The design of this structure differed for N_2 and CO_2 due to their distinct densities. Nitrogen, being slightly less dense than air, required the labyrinth configuration shown in Fig. 1a, whereas CO_2—denser than air—required the configuration shown in Fig. 1b. In both cases, the structures were built using natural stone elements and channelled the gas along specific pathways to ensure adequate heating and uniform exposure of the samples.

3. Results and discussion

3.1. Colour analysis of sandstone

The thermal treatments produced systematic changes in the optical response of the silicate matrix as a function of atmosphere and temperature (Fig. 2a). Quantitative analysis in the CIELAB space shows that both variables control the evolution of the optical state. Principal component analysis (PCA) of the L*, a* and b* coordinates reduces the colourimetric dataset to a dominant axis (PC1) that tracks the progression of the thermally induced transformations. Consequently, PC1 can be interpreted as an optical indicator of the underlying mineralogical evolution rather than as a purely descriptive colour parameter. While the present study focuses on macroscopic colour evolution using CIELAB coordinates, more advanced optical approaches have been proposed for analysing complex optical signals at higher spatial resolution, including noise reduction and phase-unwrapping strategies in heterogeneous materials [11]. Such approaches may provide complementary insight into microscale optical variability, although they fall beyond the scope of the present work.

Under oxidizing conditions (air), PC1 increases progressively with temperature. This behaviour is consistent with the stabilization of Fe^{3+}-rich phases. The optical response correlates with the formation of hematite, whose electronic transitions generate increased reflectance in the red spectral region. The results therefore indicate that the optical trajectory measured by PC1 reflects the progressive oxidation of iron-bearing precursor phases during heating.

In contrast, samples treated under N_2 and CO_2 follow the opposite optical trajectory. The decrease in PC1 indicates progressive darkening of the matrix, associated with the stabilization of mixed-valence Fe^{2+}/Fe^{3+} assemblages. The behaviour is consistent with magnetite formation under reduced oxygen partial pressure. Increasing temperature enhances the extent of reduction, particularly in N_2, where the lowest oxygen availability promotes the highest magnetite fraction. The optical

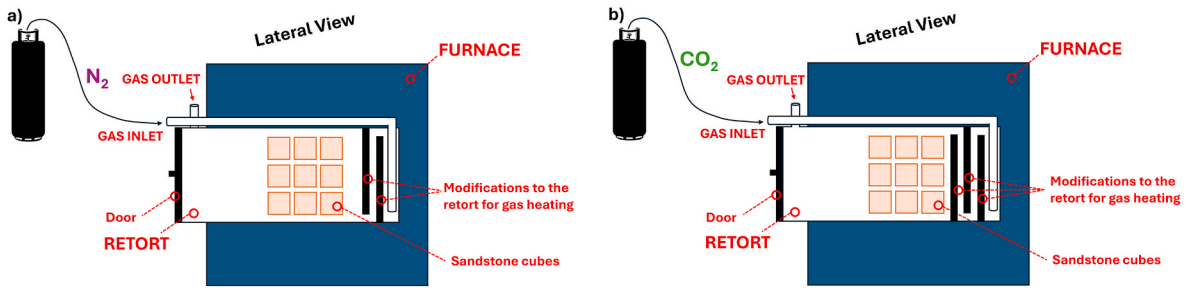

Fig. 1. Modifications to the retort to achieve homogeneous stone colouration. (a) Labyrinth structure designed for N_2, considering its lower density than air. (b) Labyrinth structure designed for CO_2, considering its higher density than air. Both modifications direct the gas flow to ensure adequate heating before contact with the samples.

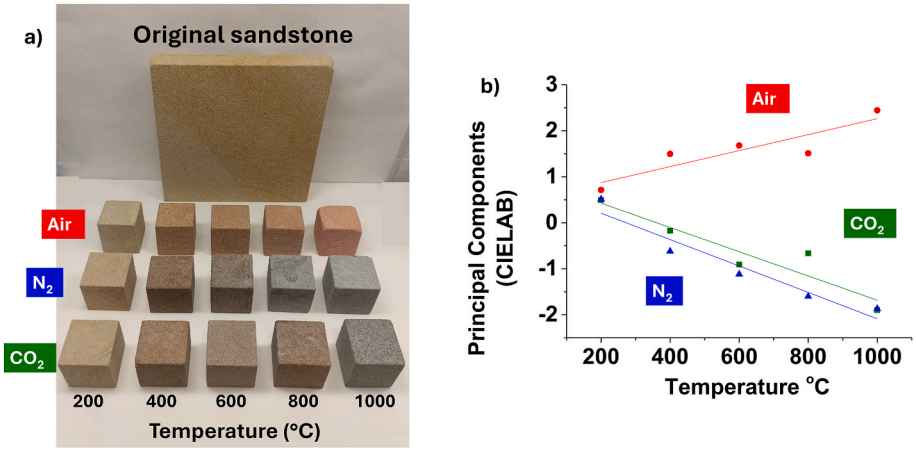

Fig. 2. (a) Representative samples after thermal treatment under 3 atm (air, N_2 and CO_2) at five temperatures (200–1000 °C). (b) Evolution of PC1 derived from PCA of CIELAB coordinates as a function of temperature and atmosphere.

evolution therefore reflects atmosphere-controlled redox equilibria rather than surface effects [5].

The magnetic signatures observed under each atmosphere closely mirror the macroscopic optical evolution, confirming that colour development is directly linked to atmosphere-controlled iron-oxide phase assemblages. This establishes a direct relationship between processing atmosphere, phase stability and optical response. While macroscopic colour provides a practical and sensitive indicator of these changes, it does not directly resolve phase equilibria. Therefore, the optical evolution is interpreted in conjunction with mineralogical, geochemical and magnetic data, which provide independent evidence of the underlying transformations. A fully quantitative thermodynamic description would require complementary approaches beyond the scope of the present study.

3.2. Matrix evolution and phase transformations

The mineral composition of the samples heated in air (O_2-rich), nitrogen (N_2), and carbon dioxide (CO_2) atmospheres revealed a consistent pattern in the thermal evolution of the sandstone, although specimens heated in air displayed slightly different characteristics compared to those heated in reduced-oxygen atmospheres.

3.2.1. Petrography

Thin sections of samples heated under different atmospheres show a broadly comparable sequence of thermally induced mineralogical transformations (Fig. 3). With increasing temperature, the sandstone matrix undergoes progressive iron-oxide development, following a characteristic trend: initial formation of hematite (Fe_2O_3), followed by coexistence of hematite and magnetite, and finally the predominance of magnetite (Fe_3O_4) at the highest temperatures. The main distinction among atmospheres is the temperature range over which these phases appear and the relative abundance of each.

In the samples heated in air, hematite remains the dominant iron oxide up to 1000 °C, and magnetite forms only in minor amounts. This behaviour agrees with petrographic and magnetic evidence indicating more limited reduction pathways under O_2-rich conditions. In contrast, samples heated in CO_2 and especially in N_2—both atmospheres with restricted oxygen availability—show a markedly greater development of magnetite. The N_2 series displays the highest abundance of sub-idiomorphic to idiomorphic magnetite crystals at 1000 °C, in agreement with the magnetic measurements presented later in the manuscript, where N_2 produces by far the strongest magnetite signature.

These qualitative petrographic observations align with the physical-property trends discussed in the following section and establish the basis for understanding the colour variations described earlier.

Petrographic comparison of unheated samples (25 °C) with those heated to 400 and 1000 °C reveals the spatial and mineralogical progression of iron-oxide formation. Hematite begins to develop below ~400 °C through thermal alteration of clay minerals within the matrix, forming cryptocrystalline aggregates that impart reddish hues. These aggregates increase with temperature until ~600 °C, after which they progressively diminish. Between ~600 and 1000 °C, hematite is increasingly replaced by opaque, idiomorphic magnetite crystals that grow within the clay-rich matrix, occupying the space formerly occupied by hematite and phyllosilicates. This transition is responsible for the grey to black tones developed in reduced-oxygen atmospheres.

3.2.2. Mineralogy

The sandstone is composed primarily of a quartz-rich framework

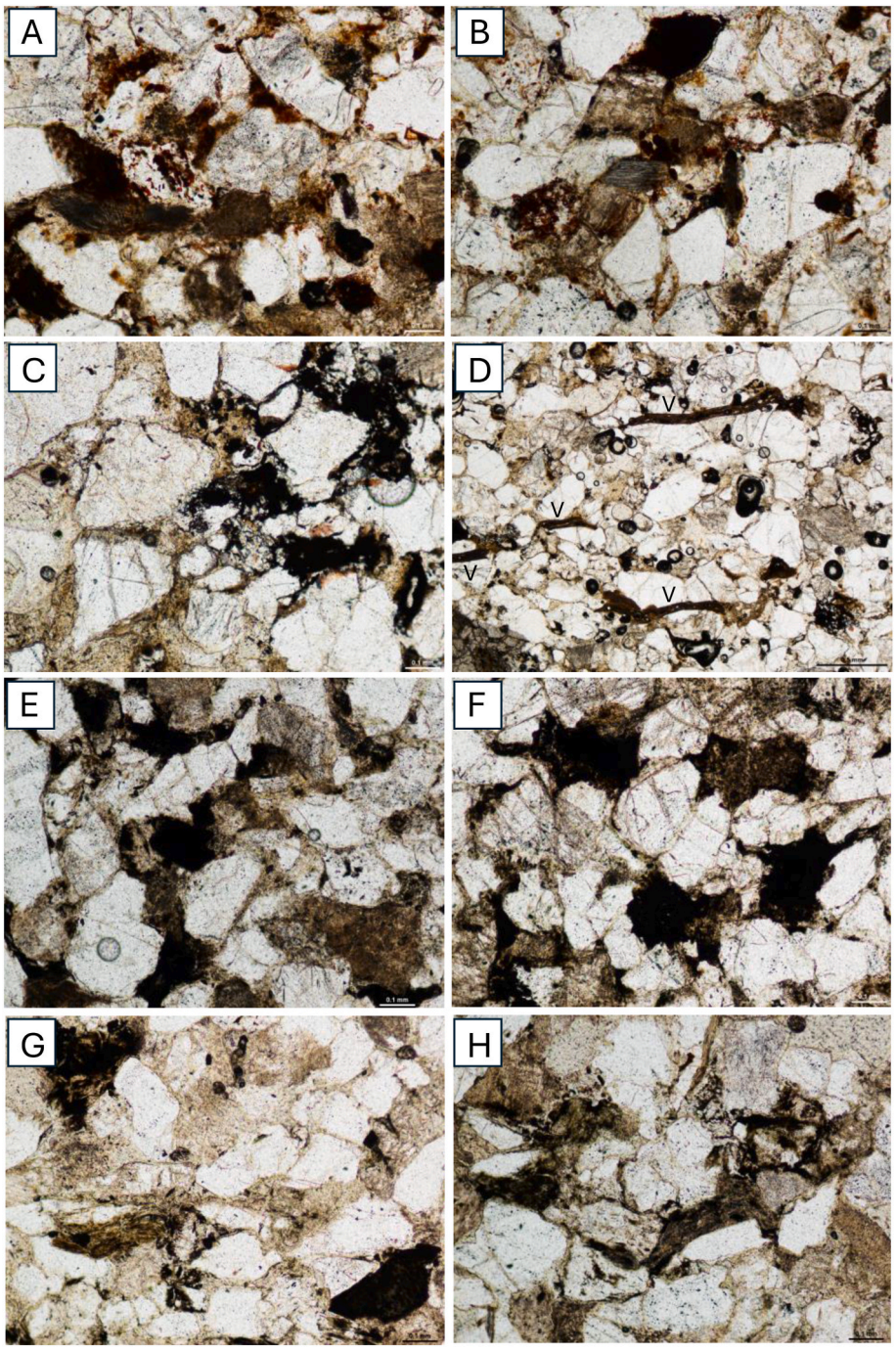

Fig. 3. Microphotographs of thin sections of sandstone samples heated to different temperatures and atmospheres. A–B: 1000 °C, air (O_2-rich). Note the reddish hematite-rich domains and the presence of subhedral opaque magnetite. C–D: 1000 °C, air (O_2-rich). Hematite remnants coexist with widespread neoformation of opaque magnetite crystals; elongated vitrified plant remains (V) are visible. E–F: 1000 °C, CO_2. Abundant idiomorphic magnetite crystals; hematite is scarce or absent. G–H: 1000 °C, N_2. Widespread idiomorphic magnetite; hematite is not preserved.

(61–72 wt%) with subordinate feldspars (11–17 wt%), while the sedimentary matrix consists of 9–26 wt% clay minerals, mainly phyllosilicates of the muscovite and kaolinite groups (Table 1). Phase proportions were estimated from normalized diffraction peak intensities and should be interpreted as relative indicators of mineralogical evolution rather than absolute quantitative values. The framework minerals (quartz and feldspars) exhibit only minor changes in abundance with heating, whereas the clay fraction undergoes a pronounced decline—up to ~75% at high temperatures under all atmospheric conditions (Table 1).

Values below the detection limit should be interpreted cautiously. This behaviour is reflected in the XRD patterns. Peaks associated with kaolinite and micas progressively decrease in intensity, resulting in an apparent relative enrichment in quartz and feldspars in the semi-quantitative diffractograms (Fig. 4). A slight initial increase in clay-mineral detection between ~200 and 400 °C (e.g., from 19.9% to 18.5%) is likely related to improved crystallinity or enhanced recognition of phyllosilicate phases. Above 400–600 °C, a marked decline occurs (e.g., from 13.2% to 5.1% at 1200 °C in air), corresponding to dehydration, dehydroxylation and structural collapse of clays along the kaolinite → metakaolinite → mullite transformation pathway [12,13].

Feldspars show more complex behaviour. Their apparent concentration may increase as Al–Si is redistributed from thermally

Table 1
Relative phase proportions derived from bulk XRD patterns based on normalized diffraction peak intensities. Values represent semi-quantitative (weight %) indicators of mineralogical evolution and not absolute phase abundances.

Sample	Temperature (°C)	Atmosphere	Quartz (%)	Clay minerals (%)	Feldspar (%)	Hematite (%)	Magnetite (%)
Air-25	25	Air	72.2	9.6	17.8	0.3	0.1
Air-200	200	Air	61.2	19.9	17.9	0.8	0.3
Air-400	400	Air	71.9	18.5	8.6	0.5	0.5
Air-600	600	Air	77.7	13.2	8.7	0.2	0.2
Air-800	800	Air	85.1	6.2	7.9	0.5	0.3
Air-1000	1000	Air	77.2	9.9	12.2	0.4	0.3
Air-1200	1200	Air	92.2	5.1	1.5	0.6	0.5
CO_2-25	25	CO_2	72	13.7	13.6	0.5	0.3
CO_2-200	200	CO_2	75.2	16.7	7.6	0.3	0.3
CO_2-400	400	CO_2	80.9	8.9	9.2	0.6	0.4
CO_2-600	600	CO_2	76.6	4.8	18.1	0.4	0.1
CO_2-800	800	CO_2	79.4	5.1	11.8	3.4	0.3
CO_2-1000	1000	CO_2	77.2	5.5	16	0.7	0.5
N_2-25	25	N_2	61.2	26.8	11.1	0.5	0.3
N_2-200	200	N_2	65.2	11.3	22.9	0.5	0.2
N_2-400	400	N_2	44.6	15.3	39	0.5	0.6
N_2-600	600	N_2	70.3	<DL	29.2	0.4	0.1
N_2-800	800	N_2	68.9	6.3	24	0.5	0.4
N_2-1000	1000	N_2	77	10.3	11.8	0.6	0.3

<DL: below detection limit (~1–4 wt%).

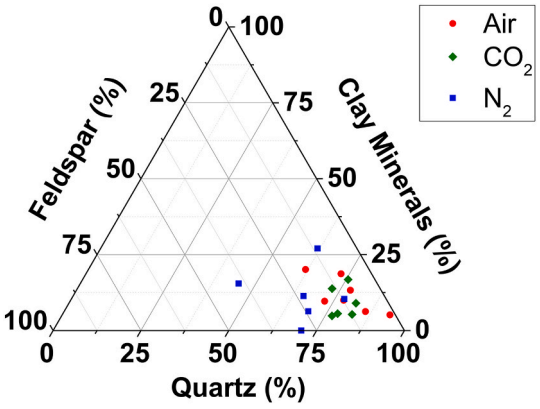

Fig. 4. Ternary diagram showing the relative proportions of quartz, feldspar and clay minerals (wt%, normalized to 100%) in sandstone samples heated under different atmospheres (air, CO_2 and N_2). Each point represents the mineralogical composition obtained by semi-quantitative XRD analysis. Samples heated under CO_2 and N_2 generally exhibit lower clay-mineral contents and relative enrichment in quartz compared with those heated in air, reflecting the progressive thermal destruction of phyllosilicates.

decomposed clays, particularly under atmospheres that limit oxidation. Such mineralogical reorganization reflects the typical response of feldspathic sandstones to sustained thermal exposure.

Iron-oxide phases occur mainly as coatings, intergranular films and microcrystalline aggregates. Under these conditions, their diffraction peaks are largely masked by the dominant quartz and feldspar reflections. The detection limit for iron oxides in bulk XRD is approximately 1–4 wt%, and phases below this threshold cannot be reliably quantified. Consequently, bulk XRD does not resolve iron oxides as independent crystalline phases, and their presence is inferred primarily through petrographic observations and magnetic measurements rather than through peak quantification. This behaviour is widely reported in ferruginous sandstones and other silicate matrices containing pigmentary iron oxides [14–16].

The mineralogical evolution of the sandstone under air, CO_2 and N_2 follows patterns characteristic of thermally stressed quartz-rich and clay-rich lithologies: relative enrichment in quartz due to the destruction of less stable phases, drastic reduction of phyllosilicates, partial feldspar reorganization and atmosphere-dependent development of Fe oxides. Collectively, these changes reflect progressive dehydration, dehydroxylation, partial recrystallization and structural reorganization as temperature increases.

Therefore, XRD results are used here primarily to support qualitative and semi-quantitative interpretation of mineralogical trends, in combination with petrographic and magnetic evidence. The apparent differences between bulk XRD results and petrographic observations can be attributed to the distinct resolution and sensitivity of the techniques. While petrographic analysis reveals iron oxides as coatings and microcrystalline phases distributed within the matrix, their low abundance, low crystallinity and fine dispersion limit their detectability in bulk XRD patterns, where dominant quartz and feldspar reflections mask minor contributions. The two approaches should therefore be considered complementary rather than contradictory, providing information at different scales of observation.

3.2.3. *Elemental geochemistry*

Elemental composition was analysed as an additional indicator of matrix evolution during thermal treatment. Variations in major oxides reflect the redistribution of elements associated with dehydration, dehydroxylation and solid-state reactions occurring during heating. Clear atmosphere-dependent and temperature-dependent trends are observed across the experimental series (Table 2), consistent with the phase transformations identified by petrography and magnetic analyses.

A PCA was applied to standardized concentrations of major oxides (SiO_2, Al_2O_3, K_2O, Fe_2O_3, Na_2O, TiO_2, MgO) and organic carbon (C_{org}). The first three components explain 86% of the total variance, indicating that the main compositional trends associated with thermal treatment are captured.

The first principal component (PC1, 51% variance) reflects a contrast between SiO_2 and the group of Al_2O_3, Fe_2O_3, MgO and K_2O. This behaviour is consistent with the progressive breakdown of phyllosilicates and the relative enrichment of the quartz framework with increasing temperature. Differences observed between air and N_2/CO_2 conditions suggest an influence of oxygen availability on these compositional trends.

The second component (PC2, 18% variance) is dominated by organic carbon and shows a strong correlation with temperature (Fig. 5b). The decrease in C_{org} is consistent with progressive thermal degradation of organic residues and can be used as an indicator of treatment severity.

The third component (PC3, 16% variance) is associated with variations in minor oxide contributions, particularly TiO_2 and alkali oxides. This component may reflect the relative enrichment of more refractory

Table 2
Elemental composition of samples at different temperatures (25 °C to 1000–1200 °C) and heating atmospheres (air, CO_2, N_2).

Sample	Temperature (°C)	Atmosphere	SiO_2	Al_2O_3	K_2O	Fe_2O_3	Na_2O	TiO_2	MgO	C_{org}
Air-25	25	Air	90.5	5.2	1.38	0.73	0.34	0.32	0.14	1.05
Air-200	200	Air	89.83	5.58	1.54	0.79	0.63	0.22	0.15	0.94
Air-400	400	Air	89.45	5.89	1.55	0.76	0.4	0.28	0.16	0.81
Air-600	600	Air	90.03	5.55	1.45	0.75	0.38	0.27	0.15	0.05
Air-800	800	Air	91.44	4.62	1.25	0.46	0.65	0.2	0.11	0.05
Air-1000	1000	Air	90.47	4.91	1.16	0.54	0.61	0.28	0.15	0.07
Air-1200	1200	Air	90.23	5.72	1.37	0.63	0.44	0.27	0.17	0.03
CO_2-25	25	CO_2	88.67	6.16	1.55	0.86	0.35	0.27	0.2	1.44
CO_2-200	200	CO_2	89.47	5.68	1.54	0.76	0.48	0.25	0.14	1.21
CO_2-400	400	CO_2	88.15	6.18	1.68	0.93	0.46	0.31	0.2	0.96
CO_2-600	600	CO_2	88.93	6.16	1.59	0.83	0.43	0.42	0.19	0.17
CO_2-800	800	CO_2	85.65	6.25	1.64	1.02	0.47	0.5	0.15	0.04
CO_2-1000	1000	CO_2	89.07	5.9	1.41	0.95	0.62	0.45	0.17	0.05
N_2-25	25	N_2	88.88	6.65	1.86	0.85	0.64	0.22	0.17	0.63
N_2-200	200	N_2	88.56	6.25	1.65	0.77	0.65	0.27	0.19	0.61
N_2-400	400	N_2	88.47	6.24	1.74	0.8	0.63	0.27	0.17	0.47
N_2-600	600	N_2	88.48	6.28	1.59	0.79	0.59	0.27	0.2	0.05
N_2-800	800	N_2	88.79	6.35	1.73	0.79	0.67	0.23	0.18	0.08
N_2-1000	1000	N_2	88.08	6.64	1.65	0.86	0.6	0.48	0.21	0.07

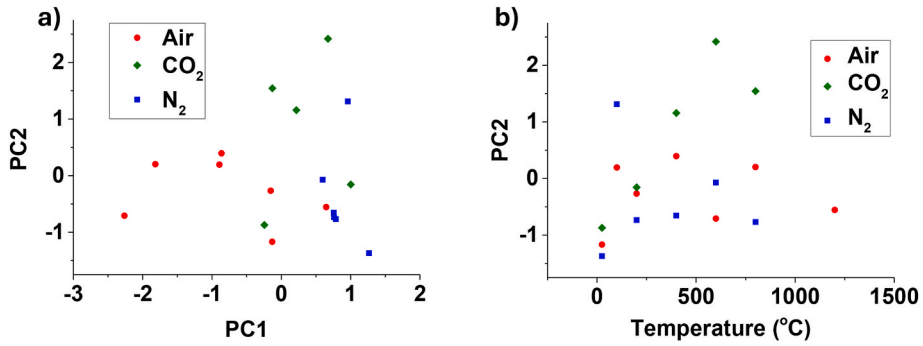

Fig. 5. PCA analysis of elemental composition. (a) PC1 vs PC2 showing separation according to atmosphere (PC1) and treatment severity (PC2). (b) Correlation between PC2 and temperature indicating progressive thermal degradation of organic matter.

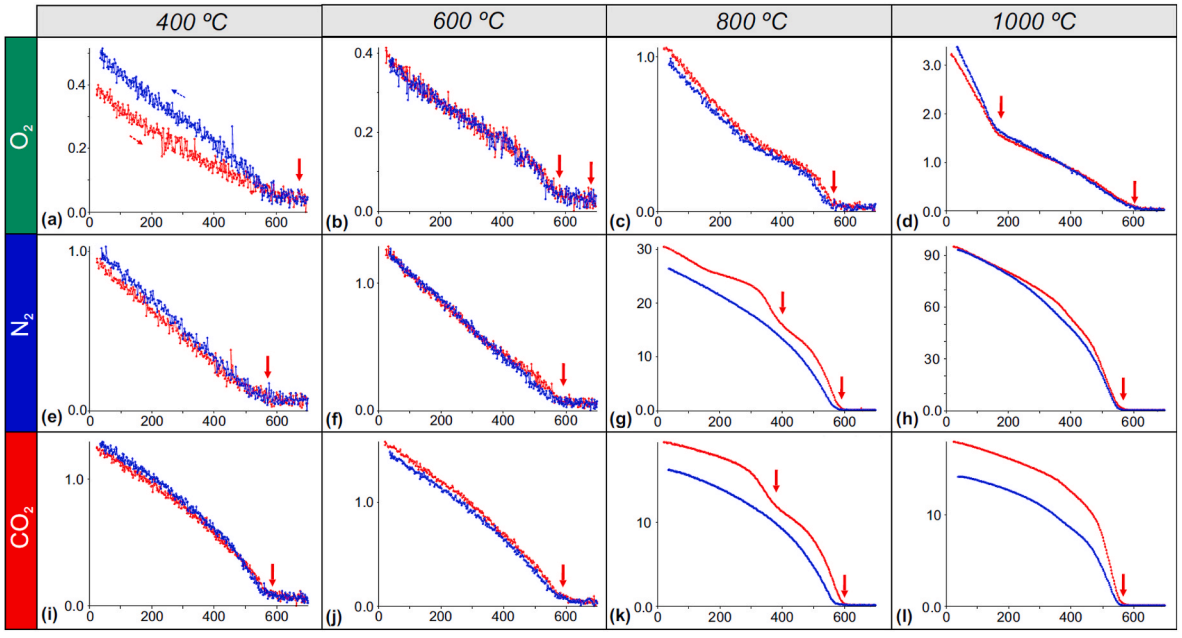

Fig. 6. Thermomagnetic curves (magnetization vs. temperature) of sandstone samples heated at 400, 600, 800 and 1000 °C under 3 atm: air (a–d), N_2 (e–h) and CO_2 (i–l). Red and blue curves correspond to heating and cooling runs, respectively. Red arrows mark key ferromagnetic transitions discussed in the text (e.g., Curie temperatures of magnetite and Néel temperatures of hematite). Note the strong increase in magnetite production in N_2, and the formation of a high-coercivity phase in air at 800–1000 °C, absent in N_2 and CO_2.

phases as less stable components are progressively transformed during heating. Such behaviour is consistent with redistribution processes linked to clay-mineral breakdown and the formation of secondary oxide phases, although PC3 primarily captures statistical correlations rather than a single well-defined transformation mechanism.

The distribution of samples in PC1–PC2 space is consistent with increasing thermal treatment severity, with temperature primarily influencing PC2 and atmosphere influencing PC1 (Fig. 5a).

Overall, the PCA results support the presence of two main contributions to the observed compositional variability: (i) a temperature-related transformation associated with dehydration and organic-matter loss, and (ii) an atmosphere-dependent contribution linked to changes in iron-bearing phases. These trends are consistent with the petrographic, magnetic and optical observations, supporting a bulk modification of the silicate matrix during thermal processing.

3.3. Magnetic properties

Magnetic measurements were used as an independent tool to track iron-oxide transformations during thermal treatment, providing phase-sensitive information that complements petrographic and geochemical analyses.

Fig. 6 presents the thermomagnetic curves of samples heated from 400 to 1000 °C under air, N_2 and CO_2 atmospheres. The 25 and 200 °C curves are not shown because their magnetic signals are extremely weak and noisy, reflecting the very low concentration of ferromagnetic minerals in the unheated sandstone. Among all series, the samples heated in air consistently exhibit the lowest magnetization intensities, whereas those heated under N_2 and CO_2 show progressively stronger ferromagnetic responses.

At room temperature (25 °C), the hyperbolic form of the heating curves (not shown) indicates a predominantly paramagnetic behaviour, consistent with the presence of clay minerals and phyllosilicates (Section 3.2.2). No clear ferromagnetic phase can be distinguished in the unburned sandstone due to its exceedingly low magnetic content.

At 400 °C, hematite can be identified in the air-heated samples, with Néel temperatures (TN) near ~670 °C (Fig. 6a). In contrast, the corresponding N_2 and CO_2 samples at 400 °C (Fig. 6e and i) are already dominated by magnetite, with Curie temperatures (TC) near ~580 °C. Although magnetite appears in very low concentrations at this stage, its magnetic behaviour is sufficiently strong to mask the contribution of hematite. This is expected because hematite is approximately **200 times less magnetic** than magnetite for the same concentration [17]. Importantly, the reddish hues observed in the samples confirm the presence of hematite even when its magnetic signal is suppressed.

Atmosphere-dependent development of magnetite. Above 600 °C in air, and above 400 °C in the N_2 and CO_2 series, the presence of magnetite becomes progressively more visible, as indicated by the sharp increase in magnetization during heating. The strongest effect occurs in N_2: (i) At 1000 °C, the N_2 sample produces 32 times more magnetite than its air-heated counterpart (Fig. 6h vs. 6d); (ii) and almost 6 times more than the CO_2 sample (Fig. 6l).

These results confirm that the type of atmosphere is a key factor controlling the formation and abundance of magnetite, in agreement with the petrographic observations (Section 3.2.1) and with the atmosphere-dependent geochemical gradients revealed by PCA (Section 3.2.3).

The magnetic signatures observed under each atmosphere closely mirror the macroscopic colour evolution, confirming that colour development is directly linked to atmosphere-controlled iron-oxide phase assemblages rather than to superficial effects.

Formation of a high-coercivity ferromagnetic phase (ε-Fe_2O_3) in air.

In the air-heated series between 800 and 1000 °C, an additional thermally stable ferromagnetic phase appears, with reversible Curie temperatures between 175 and 200 °C. Its IRM acquisition curve at 1000 °C (Fig. 6d) does not saturate at 1 T, indicating the presence of a high-coercivity mineral. This behaviour is consistent with the formation of epsilon iron oxide (ε-Fe_2O_3) [18,19], a rare phase that develops under strongly oxidizing conditions and is characterized by: very high coercivity, reversible TC in the 175–200 °C range, and wasp-waisted hysteresis cycles.

This ε-Fe_2O_3 phase does not appear in N_2 or CO_2 samples (Fig. 6g and k). Instead, these samples show heating-curve inflections around ~400 °C, suggesting the presence of cation-substituted magnetite (e.g., Ti-, Al- or Mg-bearing). This interpretation agrees with the PC3 behaviour described in Section 3.3.3, where TiO_2 increases relative to other oxides under N_2 and CO_2.

Hysteresis and IRM acquisition curves. Magnetic changes at temperatures above 800 °C are especially prominent in air-heated samples (Fig. 7a–c). The hysteresis cycle at 1000 °C (Fig. 7b) develops a pronounced wasp-waisted shape [20], characteristic of mixtures of magnetite with a high-coercivity phase—consistent with ε-Fe_2O_3 formation.

At 1200 °C, this high-coercivity phase disappears (Fig. 7c and d), leaving magnetite as the dominant ferromagnetic mineral, correlating with the dark-grey colour observed macroscopically.

In contrast, the IRM acquisition curves for N_2 and CO_2 samples at 600–1000 °C (Fig. 8e and f) saturate at 150–200 mT, indicating that their magnetic properties are overwhelmingly dominated by magnetite, without evidence for high-coercivity phases. This absence of ε-Fe_2O_3 formation under N_2 and CO_2 atmospheres can be attributed to the thermodynamic conditions associated with reduced oxygen availability. The stabilization of ε-Fe_2O_3, a metastable Fe^{3+}-rich phase, requires highly oxidizing environments. Under inert or low-oxygen conditions, the system shifts towards mixed-valence or reduced iron oxide assemblages, such as magnetite, which are thermodynamically more stable at lower oxygen partial pressures. Consequently, the oxygen-deficient atmospheres used in this study do not favour the formation of ε-Fe_2O_3.

3.4. Compressive strength of sandstone

To evaluate whether the thermal treatment alters the bulk mechanical behaviour of the material, uniaxial compressive-strength tests were performed on samples treated under air, N_2 and CO_2 atmospheres at different temperatures. As temperature increased from ambient values to approximately 600 °C, the compressive strength showed a gradual improvement, in agreement with previous studies [5]. This intermediate strengthening can be attributed to the partial closure of pre-existing microcracks, relaxation of residual stresses and improved grain-to-grain contact within the matrix. These effects enhance mechanical cohesion before the onset of significant thermal degradation processes.

Beyond 600 °C, however, this trend reverses (Fig. 8). Continued heating leads to the formation of new microcracks driven by thermal expansion mismatch, dehydration and structural breakdown of the matrix, resulting in a progressive decrease in compressive strength, consistent with general thermal degradation processes reported for silicate rocks, including microstructural changes associated with dehydration and thermal stress [21–24]. Importantly, the temperature-dependent behaviour was similar across all 3 atm, indicating that atmospheric composition has little influence on the mechanical response of the sandstone under the studied conditions, despite its strong effect on optical behaviour.

Overall, the results indicate that compressive strength remains within the same order of magnitude as that of the untreated material across the explored temperature range. These observations suggest that thermal treatment primarily affects optical behaviour, while no evidence of catastrophic mechanical degradation is observed. The mechanical data are therefore presented to verify the preservation of bulk integrity, whereas a detailed mechanistic analysis of strength evolution is beyond the scope of the present study. This behaviour aligns with broader approaches in sustainable materials engineering, where

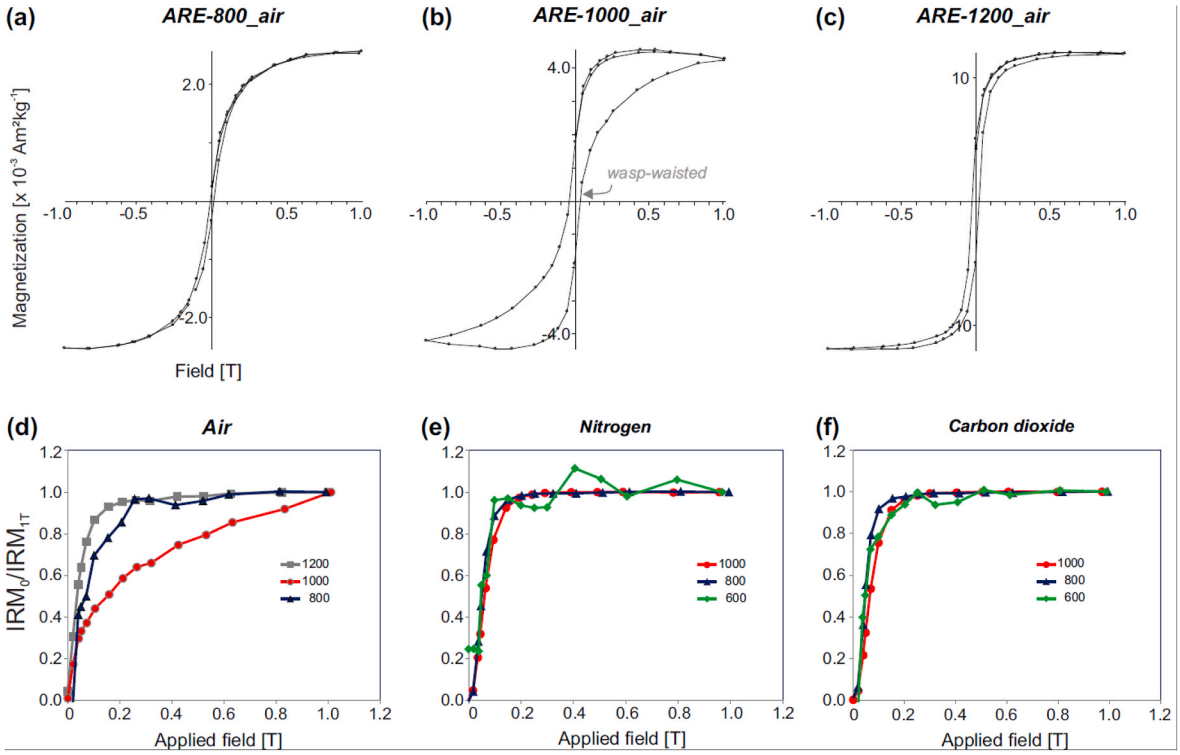

Fig. 7. (a–c) Corrected hysteresis cycles of samples heated in air at 800, 1000 and 1200 °C. The 1000 °C cycle shows a characteristic wasp-waisted shape, indicative of a high-coercivity phase (ε-Fe_2O_3). (d–f) Normalized IRM acquisition curves for air, N_2 and CO_2 samples, showing rapid saturation (150–200 mT) in N_2 and CO_2, consistent with dominantly magnetite behaviour.

a)

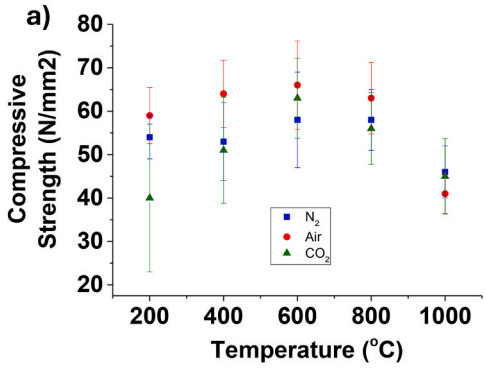

b)

Temp. (°C)	N_2 Compressive Strength (N/mm²)	N_2 SD	Air Compressive Strength (N/mm²)	Air SD	CO_2 Compressive Strength (N/mm²)	CO_2 SD
200	54.00	5.00	59.00	6.45	40.00	17.03
400	53.00	9.00	64.00	7.72	51.00	12.23
600	58.00	11.00	66.00	10.19	63.00	9.19
800	58.00	7.00	63.00	8.25	56.00	8.26
1000	46.00	6.00	41.00	4.59	45.00	8.70

* Original sandstone's compressive strength (N/mm²) = 48 ± 4.49 MPa

Fig. 8. (a) Evolution of compressive strength in sandstones heated to different temperatures (200–1000 °C) under N_2 (blue), air (green) and CO_2 (red). (b) Summary of compressive-strength values (mean of ten replicates ± standard deviation).

functional properties are tailored through controlled processing while maintaining structural integrity, as also discussed in thermally managed material systems [25].

4. Conclusions

Thermal treatment under controlled gas atmospheres induces systematic petrographic, mineralogical, magnetic and geochemical transformations in the studied sandstone, with clear differences in both temperature thresholds and transformation pathways depending on the atmosphere employed (air, CO_2 or N_2). Iron-oxide evolution follows a temperature-dependent sequence, progressing from hematite formation at moderate temperatures to mixed hematite–magnetite assemblages, and ultimately to magnetite-dominated systems at higher temperatures, particularly under reduced-oxygen atmospheres (CO_2 and especially N_2). In contrast, air-heated samples develop an additional high-coercivity iron-oxide phase between 800 and 1000 °C, consistent with the magnetic signatures attributed to ε-Fe_2O_3.

These atmosphere-dependent iron-oxide assemblages constitute the primary control on the distinct colour pathways observed. While substantial mineralogical modifications occur within the clay-rich matrix—where phyllosilicates decrease by up to ~75%—framework quartz and feldspar grains remain largely unaffected. Despite these internal transformations, uniaxial compressive-strength testing indicates that the mechanical performance of the thermally treated sandstone remains within the same order of magnitude as that of the untreated material.

Geochemical analyses, supported by multivariate statistical treatment, capture these transformations with higher sensitivity than bulk XRD alone. Principal component analysis reveals two dominant and orthogonal trends: a universal thermal axis associated with organic-matter loss, and an atmosphere-dependent axis linked to iron-oxide

formation and SiO_2 redistribution. Together, these results support the conclusion that oxygen availability, rather than temperature alone, is a key parameter governing iron-oxide evolution and colour development during thermal processing.

From an engineering perspective, this study establishes a practical, scalable and dye-free route for tuning the optical properties of sandstone through controlled temperature–atmosphere processing. The approach is chemically additive-free and capable of generating a wide range of stable and reproducible optical states from a single raw material source without evidence of catastrophic mechanical degradation. Importantly, the results demonstrate that atmosphere-controlled colour tuning in natural stone is inherently a process-engineering challenge, in which reactor design and gas-flow management are as critical as temperature and material composition. This framework expands the functional design space of natural silicate materials and provides a process-based basis for tuning optical properties through controlled thermal treatment.

Open Data

Open Data is available at https://riubu.ubu.es/handle/10259/5684 under the name "UBU-Polymers Research Group 12122025".

Declaration of competing interest

The authors declare that they have no known competing financial interests or personal relationships that could have appeared to influence the work reported in this paper.

Acknowledgments

We gratefully acknowledge the financial support provided by all funders. Authors S. Vallejos and Á. Carrancho received Grant PID2023-147301OB-I00 and Grant PID2024-159094NB-I00, respectively, funded by MICIU/AEI/10.13039/501100011033 and FEDER. The financial support provided by Fondo Europeo de Desarrollo Regional-European Regional Development Fund (FEDER, ERDF) and Regional Government of Castilla y León -Consejería de Educación, Junta de Castilla y León- (BU025P23 and BU037P23) is gratefully acknowledged. This work was supported by the Regional Government of Castilla y León (Junta de Castilla y León) and by the Ministry of Science and Innovation MICIN and the European Union *NextGenerationEU* PRTR. Author Saul Vallejos received grant BG22/00086 funded by Spanish Ministerio de Universidades.

References

[1] Gareev KG. Diversity of iron oxides: mechanisms of formation, physical properties and applications. Magnetochemistry 2023;9:119. https://doi.org/10.3390/magnetochemistry9050119.

[2] Tomás R, Benavente D, Martínez-Ibáñez V, Garrido ME. How do high temperatures affect rock properties? A comprehensive review of experimental thermal effects and underlying mechanisms. Eng Geol 2025;357:108323. https://doi.org/10.1016/j.enggeo.2025.108323.

[3] Ram BK, Das R, Mishra DA. Thermal treatment induced damage mechanisms of rock materials and their influence on physico-mechanical properties: a review. Earth Sci 2025. https://doi.org/10.1007/s12665-025-12300-6.

[4] Hajpál M. Changes in sandstones of historical monuments exposed to fire or high temperature. Fire Technol 2002;38:373–82. https://doi.org/10.1023/A:1020174500861.

[5] Yu J, Chen SJ, Chen X, Zhang YZ, Cai YY. Experimental investigation on mechanical properties and permeability evolution of red sandstone after heat treatments. J Zhejiang Univ - Sci 2015;16:749–59. https://doi.org/10.1631/jzus.A1400362.

[6] Yin T, Chen Y, Li X, Li Q. Effect of high temperature and strain rate on the elastic modulus of rocks: a review. Int J Earth Sci 2021;110:2639–60. https://doi.org/10.1007/s00531-021-02093-x.

[7] Sha S, Rong G, Tan J, He R, Li B. Tensile strength and brittleness of sandstone and granite after high-temperature treatment: a review. Arab J Geosci 2020;13:598. https://doi.org/10.1007/s12517-020-05647-6.

[8] Peng ZX, Li BX, Deng CS. Ultrahigh-Q Fano resonance in a cavity–waveguide coupled system based on second-order topological photonic crystals with elliptical holes. Opt Laser Technol 2025;181:111617. https://doi.org/10.1016/j.optlastec.2024.111617.

[9] Grommé CS, Wright TL, Peck DL. Magnetic properties and oxidation of iron–titanium oxide minerals in Alae and Makaopuhi lava lakes, Hawaii. J Geophys Res 1969;74:5277–93. https://doi.org/10.1029/JB074I022P05277.

[10] Leonhardt R. Analyzing rock magnetic measurements: the RockMagAnalyzer 1.0 software. Comput Geosci 2006;32:1420–31. https://doi.org/10.1016/j.cageo.2006.01.006.

[11] Li K, Zhao Z, Zhao H, Zhou M, Jin L, Wang D, Wang Z, Zhang L. Three-stage training strategy phase-unwrapping method for high speckle noise. Opt Express 2024;32:48895–914. https://doi.org/10.1364/OE.544968.

[12] Pachnicz MP. Thermal effects on the structural and mechanical parameters of siliceous sandstone from the Kielce upland. Civ Environ Eng Rep 2025;35:250–71. https://doi.org/10.59440/CEER/200515.

[13] Liu S, Xu J. An experimental study on the physico-mechanical properties of rocks after high-temperature exposure. Eng Geol 2015;185:63–70. https://doi.org/10.1016/j.enggeo.2014.11.013.

[14] Ali A, Chiang YW, Santos RM. X-ray diffraction techniques for mineral characterization: fundamentals, applications and research directions. Minerals 2022;12:205. https://doi.org/10.3390/min12020205.

[15] Scheinost AC, Chavernas A, Barrón V, Torrent J. Use and limitations of second-derivative diffuse reflectance spectroscopy in the visible to near-infrared range to identify and quantify Fe oxide minerals in soils. Clays Clay Miner 1998;46:528–36. https://doi.org/10.1346/CCMN.1998.0460506.

[16] Sun J, Mailloux BJ, Chillrud SN, van Geen A, Thompson A, Bostick BC. Simultaneously quantifying ferrihydrite and goethite in natural sediments using X-ray absorption spectroscopy. Chem Geol 2018;476:248–59. https://doi.org/10.1016/j.chemgeo.2017.11.021.

[17] Evans ME, Heller F. Environmental magnetism: principles and applications of environmagnetics. San Diego: Academic Press; 2003.

[18] McIntosh G, Kovacheva M, Catanzariti G, Osete ML, Casas L. Widespread occurrence of a high-coercivity, thermally stable magnetic phase in heated archaeological materials. Geophys Res Lett 2007;34:L21302. https://doi.org/10.1029/2007GL031168.

[19] López-Sánchez J, McIntosh G, Osete ML, del Campo A, Villalaín JJ, Pérez L, Kovacheva M, Rodríguez de la Fuente O. Epsilon iron oxide: origin of the high-coercivity, low Curie temperature magnetic phase in heated archaeological materials. G-cubed 2017;18:2646–56. https://doi.org/10.1002/2017GC006929.

[20] Tauxe L, Mullender TAT, Pick T. Potbellies, wasp-waists and superparamagnetism in magnetic hysteresis. J Geophys Res Solid Earth 1996;101:571–83. https://doi.org/10.1029/95JB03041.

[21] Zhang L, Yang D, Zhao K, Zhao Y, Jin J, Wang X, Zhu L, Wang X, Li C. High-temperature effects on strengthening and degradation of mechanical properties in sandstone. Appl Energy 2024;357:122532. https://doi.org/10.1016/j.apenergy.2023.122532.

[22] Wang P, Yin T, Li X, Konietzky H. Evolution of micro-damage and degradation of macro-mechanical properties of sandstone due to thermal effects. Bull Eng Geol Environ 2023;82:83. https://doi.org/10.1007/s10064-023-03094-7.

[23] Sirdesai NN, Singh TN, Pathegama Gamage R. Thermal alterations in the poro-mechanical characteristics of sandstone: a comparative study. Eng Geol 2017;226:208–20. https://doi.org/10.1016/j.enggeo.2017.06.010.

[24] Xiao W, Zhang D, Luo W, Huang Y, Wan H, Li S. Influence of temperature on building sandstone: insights from microstructure, thermal strain and rupture crack. Constr Build Mater 2024;451:138888. https://doi.org/10.1016/j.conbuildmat.2024.138888.

[25] Yang C, Zhou Y, Wang X, Zhou Y. Sustainable high thermal conductivity composites from biomass: bio-based polyimide/microencapsulated CNTs for green thermal management. ACS Appl Polym Mater 2026;8:2762–75. https://doi.org/10.1021/acsapm.5c04260.